Solar Energy 177 (2019) 262–273

Contents lists available at ScienceDirect

Solar Energy

journal homepage: www.elsevier.com/locate/solener

Fabrication of Cu_2SnS_3 thin film solar cells by sulphurization of sequentially sputtered Sn/CuSn metallic stacked precursors

Ejarder Sabbir Hossain[a,1], Puvaneswaran Chelvanathan[b,*,1], Seyed Ahmad Shahahmadi[c], Badariah Bais[a], Md. Akhtaruzzaman[b], Sieh Kiong Tiong[c], Kamaruzzaman Sopian[b], Nowshad Amin[a,c,*]

[a] Department of Electrical, Electronics and System Engineering, The National University of Malaysia, 43600 Bangi, Selangor, Malaysia
[b] Solar Energy Research Institute (SERI), The National University of Malaysia, 43600 Bangi, Selangor, Malaysia
[c] Institute of Sustainable Energy (ISE), Universiti Tenaga Nasional (@The National Energy University), Jalan IKRAM-UNITEN, 43000 Kajang, Selangor, Malaysia

ARTICLE INFO

Keywords:
Cu_2SnS_3 solar cells
Photovoltaic technologies
Thin film deposition
SnS secondary phase

ABSTRACT

In this present work, we report a novel fabrication technique of ternary Cu_2SnS_3 (CTS) thin films by sulphurization of sequentially sputtered Sn/CuSn (elemental/alloy) stacked metallic precursors. The focal aim of our investigation is on the impact of metallic precursors' Cu/Sn ratio on the overall material properties of CTS films, which in turn, influence the photovoltaic device performance. All CTSs exhibited polycrystalline films with a mixture monoclinic CTS and orthorhombic SnS compound, p-type conductivity, and optical band gap in the range of 0.84–0.90 eV. Metallic precursor with Cu/Sn ratio of 1.09 produced optimum CTS film with post-sulphurization Cu/Sn ratio of 1.98 and highest conversion efficiency of 0.71%, respectively, despite exhibiting pronounced formation of SnS secondary phase. The correlation between XRD, Raman, and SEM-EDX outcomes revealed that CTS films from metallic precursors with Cu/Sn ratio higher than 1.09 undergo severe microstructural degradation due to Sn-loss through decomposition of volatile SnS phase and consequently, resulted in poorer absorber layer quality and lower device performance. Finally, several efficiency impeding factors are discussed and practical propostions to overcome them are presented.

1. Introduction

Cu_2ZnSnS_4 (CZTS) based quaternary absorber material has been rigorously explored in the past two decades. Consequently, record power conversion efficiencies (PCEs) of 10.04% (cell area: 1.1130 cm^2) and 11.01% (cell area: 0.2339 cm^2) have been attained for CZTS thin film solar cells up-to-date (Yan et al., 2018). However, one of the main shortcomings of CZTS material is that, it possesses a very narrow region of stable chemical potential, thus, resulting in facile formation of binary (CuS, SnS, SnS_2 and ZnS) and ternary secondary (Cu_2SnS_3) phases during crystallization process (Chen et al., 2010; Nagoya et al., 2010). Interestingly, Cu_2SnS_3 (CTS) is a ternary semiconducting compound, which has a similar crystal structure to CZTS and also has been considered as a promising candidate for thin film solar cell absorber material. CTS possesses suitable tunable band gap (0.9–1.35 eV) and p-type electrical conductivity with high optical absorption coefficient ($> 10^4\ cm^{-1}$) (Avellaneda et al., 2010; Bouaziz et al., 2011; Fernandes et al., 2010; Zhai et al., 2011) while maintaining the environmentally friendly-earth abundant elemental components. Moreover, CTS (Cu-Sn-S material system) possesses wide stable range in its chemical potential phase space, which indicates a lower probability of secondary phase formation and defect complexes (namely Cu/Zn structural disorder) during crystallization as well as wider and more flexible material processing window (temperature, pressure and composition) compared to CZTS material (Zawadzki et al., 2013). In terms of device performance of pure sulphide CTS based material (Se-free and without any Ag or Ge dopants), the current record efficiency is 4.8% achieved by Chatana et al., which was accomplished by employing sequential sputtering of Cu and SnS_2 precursors and electron beam evaporation of NaF compound, followed by sulphurization process (Chantana et al., 2017). Meanwhile, the highest efficiency obtained for none Na-doped, pure sulphide CTS device fabricated by sputtered precursor-sulphurization route was reported by Chierchia et al. with PCE of 3.05% (Chierchia et al., 2015). Based on the practical success story of CIGSSe technology

---

* Corresponding authors at: Department of Electrical, Electronics and System Engineering, The National University of Malaysia, 43600 Bangi, Selangor, Malaysia (N. Amin).

E-mail addresses: cpuvaneswaran@ukm.edu.my (P. Chelvanathan), nowshad@uniten.edu.my (N. Amin).

[1] These authors have contributed equally to this work.

https://doi.org/10.1016/j.solener.2018.10.081
Received 21 August 2018; Received in revised form 25 October 2018; Accepted 29 October 2018
Available online 15 November 2018

pioneered by Solar Frontier for both small area laboratory device and commercialized large area module production, sputtering technique possesses unparalleled advantages in comparison with all the other deposition methods (Takuya, 2017). Hence, keeping an eye on the prospective commercialization future of CTS technologies, we have consciously focused our experimental efforts towards optimizing the Sn/CuSn metallic precursor deposition using magnetron sputtering technique. This step is aimed to produce initial baseline results and serves as an empirical investigation for optimum Cu/Sn ratio, which is an important experimental pre-requisite towards the use of simple and low-cost single binary CuSn alloy target in the future. In the subsequent paragraph, a brief literature relevant to our experimental approach is reviewed as a prelude to the main research objective of our study presented herein. For an in-depth literature survey on the development of CTS thin film solar cells by physical techniques and chemical synthesis of CTS nanoparticles based on non-vacuum methods, readers are encouraged to peruse review article by Lokhande et al. and Pejjai et al., respectively (Lokhande et al., 2016; Pejjai et al., 2018).

One of the key CTS material properties, which has to be meticulously controlled in order to fabricate high quality-photovoltaic grade thin film absorber layer is the final Cu/Sn ratio. Cu-poor and Sn-rich compositions have been theoretically and experimentally identified as the optimum condition to induce p-type electrical conductivity in CTS based material (Baranowski et al., 2014). Conventionally, the Cu/Sn ratio of the sputtered precursor is controlled by modulation of sputtering process parameters, predominantly sputtering power and time. H. Zhang et al. reported Cu/Sn ratio control scheme by varying the deposition time of metallic Sn and Cu precursors sequentially using DC magnetron sputtering system (Zhang et al., 2014). On the other hand, Y. Dong et al. reported an identical control scheme for Cu/Sn ratio by using the RF sputtering system (Dong et al., 2015). Apart from deposition time parameter, variation of sputtering power of individual Cu and Sn metallic target also can be used as a control scheme for Cu/Sn ratio as demonstrated by Tang et al. (2015a). In 2016, both Bodeux et al. and Chierchia et al. groups used sputtering power control scheme to optimize the Cu/Sn ratio using sulphide-based targets of CuS and SnS instead of pure metallic form (Bodeux et al., 2015; Chierchia et al., 2015). The former group described the properties of CTS thin films with Cu-rich, Cu-poor, and stoichiometric conditions, whereas the latter reported findings on optimization of Cu/Sn ratio in the Cu-poor region only. Besides co-sputtering of dual Cu and Sn-based targets, single CuSn alloy target has been also employed as a precursor deposition route using sputtering technique (Sato et al., 2015). However, no working CTS device has been reported by using CuSn alloy target as precursor source so far. This could be due to the use of a single CuSn alloy target with a pre-defined Cu/Sn ratio, which restricts the modulation of elemental composition in the sputtered film, thus limiting the range of Cu/Sn compositional optimization possibilities during precursor deposition step. In addition to the abovementioned limitation, the use of a single CuSn alloy target with a pre-defined Cu/Sn ratio does not necessarily result in sputtered precursor with desired Cu/Sn ratio. This is due to the occurrence of preferential re-sputtering, different take-off angles and binding energy of target elements, varying angular distribution of the sputtered element, scattering, different sticking co-efficient as well as influence of target morphology, etc. (Boydens et al., 2013; Ferdaous et al., 2018; Särhammar et al., 2014; Sigmund et al., 1982).

Therefore, the primary objective of our study is to deposit and characterize sequentially sputtered Sn/CuSn metallic precursors, by employing RF-sputtering of elemental Sn target coupled with DC-sputtering of single CuSn alloy target technique. Additional elemental Sn deposition is intended to increase Sn content and subsequently tailor the overall precursors' composition to be Cu-poor, Sn-rich, with variable Cu/Sn ratio. In order to incorporate sulphur in the sputtered films, the deposited precursors were then subjected to sulphurization process, resulting in ternary CTS films. Structural, compositional, vibrational, morphological, optical, and electrical properties of CTS films were then characterized by using appropriate material characterization techniques. Finally, CTS thin film solar cells were fabricated and their photovoltaic performance parameters were recorded. Herein, we present comprehensive experimental findings on the interdependence between the intentionally varied precursors' Cu/Sn ratio, and resulting material properties of CTS thin films as well as their corresponding device performance. To the best of our knowledge, this is the first experimental investigation, which employs dual RF-DC sequentially sputtered Sn/CuSn (elemental/alloy) metallic precursor format for CTS thin film absorber layer and practical CTS photovoltaic device fabrication with the best efficiency of 0.71%.

2. Experimental technique

2.1. Sn/CuSn precursor deposition and sulphurization

Soda lime glass (SLG) substrates were ultrasonically pre-cleaned by methanol-acetone-methanol-deionized water sequence before blow-dried using N_2 jet stream, and finally heated on the hotplate at 100 °C for 10 min to remove any possible residual moisture. A 1-µm thick Mo back contact layer was deposited using a magnetron sputtering system (Kurt J. Lesker, model 4G-3RF-1DC) as described in our previous publications (Chelvanathan et al., 2017a, 2017b; Chelvanathan et al., 2015). Two-step method was carried out to fabricate the CTS absorber layer: deposition of stacked metallic precursor through sputtering and subsequent sulphurization process. Sputtering deposition chamber's base pressure was brought down to 5×10^{-6} Torr by turbomolecular pump and the working pressure during all the deposition runs was maintained at 24 mTorr by flowing 4 sccm of high purity Ar (Linde, 99.9999%) as the working gas. Stacked metallic precursors were deposited sequentially on Mo-coated SLG from elemental Sn target (Matsurf, 99.999%) by using RF mode, and then followed by CuSn alloy target (Matsurf, 99.999%) with pre-defined atomic composition of 64% Cu, and 36% Sn (Cu/Sn ratio ≈ 1.78) by DC mode. The substrates were pre-heated at 100 °C for 60 min to ensure uniform thermal heating prior to sputter deposition, and the sputtering powers for elemental Sn and CuSn alloy target were set to RF-80 W and DC-50 W, respectively. The reason for implementing low substrate heating is to promote inter-diffusions of metallic elements, subsequently, enhancing the uniformity, adhesivity, and morphological properties of sputtered films without affecting the compositional of the sputtered precursors. In order to reduce direct reaction between sulphur and elemental Sn, which inevitably leads to formation and subsequent decomposition of SnS binary compound during sulphurization process, elemental Sn layer was deposited in between Mo and CuSn layers (Pallavolu et al., 2018). In order to minimize the formation of detrimental MoS_2 interfacial layer (Akio and Takahiro, 2018; de Wild et al., 2016a; Puvaneswaran et al., 2012), which stems from the spontaneous reaction between Mo and sulphur, compact and highly (1 1 0) oriented Mo back contact is preferred to impede sulphur in-diffusion into Mo lattice (Chelvanathan et al., 2018). On the other hand, MoN and MoO_x based intermediate layers also can be grown by employing reactive sputtering or simple air annealing techniques to inhibit formation of MoS_2 layer (Chelvanathan et al., 2017a, 2017b; Kang et al., 2018). 5 different deposition time profiles for Sn sputtering from 10 to 50 min were implemented, resulting in Sn layer with increasing thickness ranging from 25 to 310 nm with the aim of having variable Cu/Sn ratio in the sputtered precursor. Table 1 summarizes the deposition time profiles, Sn and CuSn layer thickness as well as the Cu/Sn ratio of precursor and corresponding sample nomenclatures used throughout this study. Detailed material properties of as-deposited precursors are presented in Supplementary Material.

The prepared SLG/Mo/Sn/CuSn stacks were then placed into a graphite box (~10 cm^3 volume) with 120 mg sulphur and 20 mg SnS powder, which was later transferred into a quartz tube furnace (MTI-USA, model OTF-1200X) for sulphurization. SnS powder is added to

Table 1
Sn and CuSn deposition time and thickness profiles, Cu/Sn ratio and corresponding sample nomenclatures.

Deposition time (Min)		Thickness (nm)		Cu/Sn ratio of as-deposited precursor	Sample nomenclature	
Sn	CuSn	Sn	CuSn		Precursor	Sulphurized
10	75	25	750	1.5647	Sn_25	S1
20	75	65	750	1.2598	Sn_65	S2
30	75	170	750	1.0929	Sn_170	S3
40	75	260	750	1.0610	Sn_260	S4
50	75	310	750	0.9062	Sn_310	S5

suppress volatilization of Sn related compound during sulphurization process. Prior to sulphurization process, the quartz tube was purged three times by N_2 gas to remove contaminations, and the tube was pumped down to the base pressure of 100 mTorr using the 2-stage rotary pump. The internal furnace temperature was increased from room temperature (RT) to the desired sulphurization temperature of 550 °C with a fixed ramp-up rate of 25 °C/min and holding time of 60 min. Sulphurization was carried out in high purity N_2 (Linde, 99.9999%) atmosphere with working pressure of 400 Torr at 550 °C. In-situ temperature control and monitoring were carried out by a K-type thermocouple, which was connected to a digital handheld thermometer. The thermocouple was placed in close proximity to the graphite box for precise real-time temperature monitoring and feedback control, rendering temperature deviation lesser than ± 0.5% throughout the entire process. At the end of the sulphurization process, the samples were cooled to RT. Schematic diagram of the sulphurization setup used in this study is illustrated in Fig. S6 in the Supplementary Material.

2.2. CTS thin film solar cell device fabrication

CTS thin film solar cells were fabricated in substrate type architecture of SLG/Mo/CTS/CdS/i-ZnO/ITO/Ag by the following described methodology. After the completion of sulphurization process, CTS thin films were etched in a 10% (w/w) potassium cyanide, KCN solution for 2.5 min and followed by several DI water rinsing at RT. This step is carried out to remove deleterious semi-metallic phase of Cu_xS, which could have formed during sulphurization process and segregated on the films' surface. To form a p-n heterojunction, n-type CdS buffer layer was deposited by chemical bath deposition (CBD) method, following the optimized process described in our previous works (Islam et al., 2013; Yusoff et al., 2015). Precipitation chemistry and kinetics of CBD method were carefully controlled in order to deposit uniform and homogenous 50 nm thick CdS layer. A thin CdS layer is required in order to minimize parasitic absorption and maximize transmission of photons in the 300–525 nm range, which could potentially increase the current density of the device (Chelvanathan et al., 2010). To complete the device fabrication, 50 nm thick of intrinsic ZnO (i-ZnO) highly resistive transparent (HRT) layer and 350 nm thick of indium tin oxide (ITO) transparent conducting oxide (TCO) layer were deposited by sputtering technique as described in our earlier publications (Aliyu et al., 2012; Husna et al., 2012). Finally, to ensure effective photo-generated current collection, 300 nm thick Ag metal grid-front electrode was DC-sputtered at RT. Mechanical stainless steel blade scriber was used to expose the underlying Mo back electrode as well as to define individual cell, rendering an effective area of 0.25 cm^2 per each cell and 8 cells per sample. Quick drying Ag paint (TedPella Inc.) was carefully applied on the exposed Mo strip with the aim lowering the contact resistance between the probe tip and back electrode during J-V characteristics measurement.

2.3. Thin film material and device characterization

The structural and crystallographic properties of the Sn/CuSn precursor and CTS absorber layer were probed by x-ray diffraction (XRD) method using BRUKER AXS-D8 Advance at RT. XRD patterns were recorded with Cu-Kα radiation ($\lambda = 1.5408$ Å) in the 2θ range from 20° to 80° with a step size of 0.02°. Surface morphology, cross-sectional view, grain microstructures of the samples were observed and recorded by using Hitachi SU1510 scanning electron microscopy (SEM), which was operated at 3–15 kV. Compositional measurement to precisely determine the Cu/Sn ratio was carried out using Horiba EMAX 450 energy–dispersive x-ray (EDX) spectroscopy at 300 × magnification (spot size 1 mm × 1 mm) and with an accelerating voltage of 15 kV. Characterization of micro and nanoscale surface topological as well as RMS roughness of CTS films were accomplished by using NT-MDT, NTEGRA PRIMA scanning probe microscopy (SPM) in non-contact mode. Vibrational study for CTS films was performed using Thermo Scientific DXR2xi confocal micro-Raman imaging microscope, with laser excitation wavelength of 455 nm, laser power of 3 mW and laser spot size of 1 µm. An average of 8 measurements were carried out for every spot, in 3 different arbitrarily chosen areas of the samples in order to rule out spatial phase inhomogeneity. Optical property namely band gap was calculated from the reflectance measurement, which was performed using Perkin-Elmer Lambda 950 UV/VIS/NIR spectrometer equipped with a 60 mm integrating sphere from 190 to 2500 nm. Electrical properties such as carrier concentration, mobility, and resistivity of CTS films were obtained by HMS ECOPIA 3000 Hall measurement system. Measurements were performed in the dark using van der Pauw geometry with a magnetic field of 0.57 T and a probe current of 500 µA at RT. A statistically averaged value was taken for each CTS sample and the given error is the standard deviation of the mean of 30 measurements. Light J-V characteristics of solar cells were measured under AM 1.5 G illumination supplied from a AAA class SSPN-X150T solar simulator (Light Doctor Optical Corporation, Taiwan) with IVDN-250E source meter. A certified monocrystalline Si reference cell (PV Measurement Inc.) was used to match the solar spectrum and 1-sun intensity. Measurements were done at ambient air (25–30 °C), with a reverse bias to a forward bias of −0.05 to +0.8 V, step size of 10 mV and 100 ms dwell time.

3. Results and discussion

(a) **Structural properties**

Fig. 1 shows the XRD patterns for CTS thin films, which are fabricated from sulphurization of different Sn/CuSn metallic precursors with variable Cu/Sn ratio. All the sulphurized films exhibit polycrystalline characteristics with two primary sulphide based compounds of binary SnS and ternary CTS. Precise phase identification of CTS solely by XRD measurement is complicated due polymorphism characteristics of CTS material system (Oliva et al., 2017). However, by using Raman characterization technique as a complementary tool for phase identification as well as optical spectroscopy measurement, the detected CTS phase could be correlated to the monoclinic phase. Detailed results, relevant analysis and discussion pertaining to Raman and optical properties will be presented in the later sections. CTS exhibits dominant diffraction peak of (−1 3 1) orientation at 2θ ≈ 28.45°, meanwhile, SnS possesses dominant diffraction peak of (0 0 4) orientation at 2θ ≈ 32°. The obtained diffraction patterns from this study are in good agreement with the standard spectrum documented in JCPDS card no. 04-010-5719 for monoclinic CTS. Our findings are in line with Berg et al. who reported monoclinic phase for the CTS film fabricated by electrodeposition of Cu-Sn precursor and sulphurization at 550 °C (Berg et al., 2012a, 2012b). On the other hand, diffraction peaks of SnS phase are matched with JCPDS card no. 00-053-0526, which indicates SnS crystallizes in orthorhombic structure and can be identified to space group of *Pnmb*

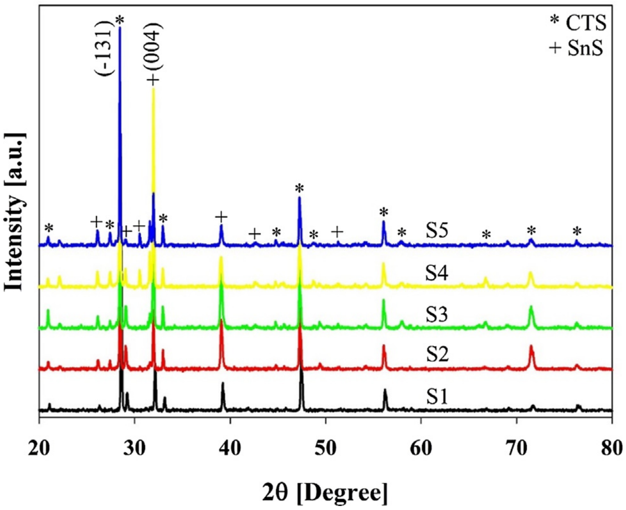

Fig. 1. XRD patterns of CTS films.

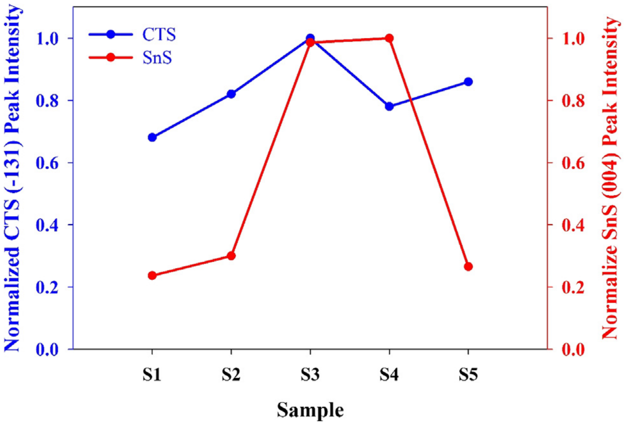

Fig. 2. Normalized XRD peak intensity of (−1 3 1) CTS and (0 0 4) SnS.

with lattice parameter of $a = 3.9803$ Å, $b = 4.3312$ Å, and $c = 11.1802$ Å. SnS binary compound by itself is a p-type semiconductor, which is currently widely studied under various research themes such as photovoltaic, photocatalytic, photodetectors, and batteries (Pejjai et al., 2017). Formation of CTS phase can be directly correlated to sulphur incorporation into Cu_6Sn_5 alloy component in the precursor by the following proposed reactions (1)–(3) by Tang et al. (2015b) as shown below:

$$2Cu_6Sn_5\ (s) + 19S(g) \rightarrow 3Cu_2S\ (s) + 8SnS_2\ (s) + 2Cu_3Sn\ (s) \quad (1)$$

$$2Cu_3Sn\ (s) + 7S\ (g) \rightarrow 3Cu_2S(s) + 2SnS_2\ (s) \quad (2)$$

$$Cu_2S\ (s) + SnS_2\ (s) \rightarrow \mathbf{Cu_2SnS_3\ (s)} \quad (3)$$

No traces of residual intermetallic Cu_6Sn_5, Cu_3Sn alloy and elemental Sn phases were detected in all sulphurized films, indicating complete conversion of metallic precursor into sulphide based compounds during sulphurization process. On the other hand, the formation of SnS phase is due to the reaction (4) between the elemental Sn component in the precursor with S and followed by a couple of irreversible decomposition reactions (5) and (6) as described below:

$$Sn\ (s) + 2S\ (g) \rightarrow SnS_2\ (s) \quad (4)$$

$$2SnS_2\ (s) \rightarrow Sn_2S_3\ (s) + 2S_{0.5}\ (g) \quad (5)$$

$$2Sn_2S_3\ (s) \rightarrow \mathbf{2SnS\ (s)} + 2S_{0.5}\ (g) \quad (6)$$

However, both of these CTS and SnS compounds co-exist in the sulphurized films with different degree of crystallinity as shown in Fig. 2, whereby the normalized diffraction peak intensity of preferred orientation for both CTS and SnS phases is plotted. Collective monotonic increase in the crystallinity of CTS as well as SnS is observed for S1, S2, and S3 and are consistent with the Cu_6Sn_5 and Sn precursor crystallinity evolution (See Fig. S4 of the Supplementary Material). However, sulphurized films of S4 and S5 show no systematic trend for CTS phase, meanwhile crystallinity of SnS phase minutely increases in S4 before severely deteriorating in S5. Based on the quantitatively observed evolution of crystallinity for both CTS and SnS, the following phenomenon is proposed to describe the probable crystallization mechanism. Since, all metallic precursors (Sn_25–Sn_310) are composed with identical CuSn alloy content and undergo parallel sulphurization process, hence, the observed different structural characteristics for sulphurized films are due to the variable elemental Sn content (thus Cu/Sn ratio, see Table 1) in the precursors.

Elemental Sn and Cu_6Sn_5 alloy have melting points of 231.9 °C and 415 °C, respectively (Fürtauer et al., 2013; Li et al., 2013; Luu et al., 2013). During sulphurization process ramp-up, these precursors are expected to be partially in Cu-Sn metal liquid and interact with sulphur atoms to form SnS and CTS. Precursor with higher Sn content is likely to form higher degree of SnS phase. However, owing to the high volatility of SnS phase at high temperature (in this case, sulphurization temperature of 550 °C), loss of elemental Sn through decomposition of SnS phase from the precursors is expected to occur (Weber et al., 2010). Higher Sn loss is expected from precursors with higher initial SnS content, which eventually would lead to degradation of SnS phase crystallinity as evident in S5 film. On the other hand, grain growth and crystallization of CTS phase are proposed to be influenced by the parallel SnS formation dynamic as depicted in Fig. 3, whereby (−1 3 1) oriented crystallite size and its corresponding full width at the half maximum (FWHM) values are plotted. The average crystallite size of the samples was calculated from the FWHM of the (−1 3 1) peak (β), using the Debye–Scherrer equation as follows:

$$D = \frac{0.94\lambda}{\beta\cos\theta} \quad (7)$$

Crystallite size gradually increases for S1, S2 and S3 before substantially decreasing in S4 and S5, which corroborates well with the observed crystallinity trend (see Fig. 2). Although secondary phase of SnS is construed as a competing phase for the CTS, increasing crystallinity of SnS in the case of S1, S2 and S3 facilitates the CTS grain growth. This is possibly due to controlled Sn-loss stemming from the optimal range of Cu/Sn ratio in the precursor. Hence, solely from CTS crystallinity and grain growth point of view, Cu/Sn ratio of 1.09 (Sn_170) is regarded as the optimum composition for Sn/CuSn metallic stacked precursor, which resulted in the optimum sulphurized film of S3.

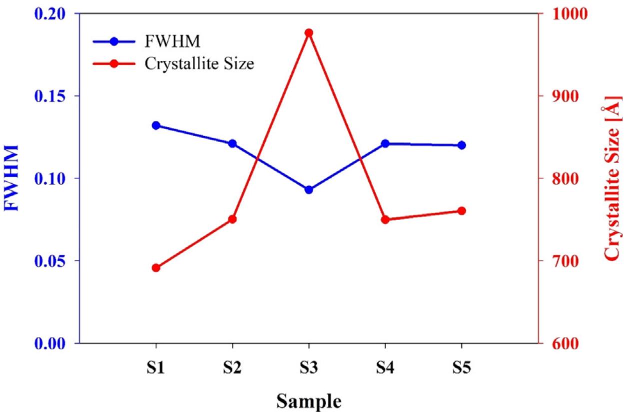

Fig. 3. FWHM and size of (−1 3 1) oriented CTS crystallite.

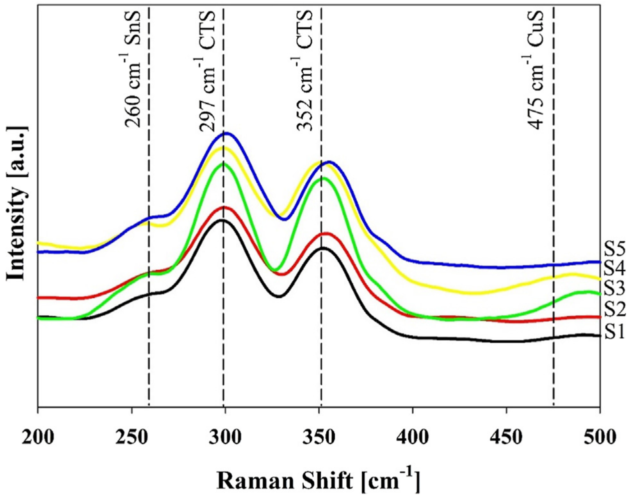

Fig. 4. Raman spectra of CTS films.

(b) **Vibrational properties**

Figs. 4 and 5 depict the overall Raman spectra (vertically shifted for clarity) and relevant normalized CTS Raman peak intensity for two distinct modes, respectively. For all films, two common dominant peaks positioned at around 297 and 352 cm^{-1} are detected as shown in Fig. 4. At a glance, the detected peaks closely resemble vibrational modes of tetragonal CTS. However, tetragonal CTS has been reported to exhibit a signature Raman peak at 338 cm^{-1} with relatively higher intensity compared to Raman modes at 297 and 351 cm^{-1}, which is not observed in our measured spectra (Fernandes et al., 2011). Furthermore, tetragonal dominant CTS thin film possesses higher XRD diffraction Bragg angle for the $(-1\,3\,1)$ preferred orientation in the range of $2\theta \approx 28.55°$, which is also not observed in our XRD measurement and analysis. Hence, by coupling both of the aforesaid observations, we can conclusively say that all sulphurized films are not composed of any tetragonal dominant CTS phase.

On the other hand, major Raman modes of monoclinic CTS has been reported to occur at 290 and 352 cm^{-1} (Berg et al., 2012a). Recently, Matsumoto et al. reported Raman modes for monoclinic CTS in the region of 290–295 cm^{-1} and 354–357 cm^{-1} (Matsumoto et al., 2016). Therefore, the CTS Raman peaks recorded in our study has a better match to the vibrational signatures of monoclinic phase and is substantiated with the previously presented XRD measurement results. Evolution of normalized CTS Raman peak intensity for 297 and 352 cm^{-1} modes as depicted in Fig. 5 clearly indicates that the S3 film possesses the highest degree of crystallinity, further validating our previous XRD results (see Figs. 2 and 3). Along with these strong peaks, the spectra also show two weak peaks located at around 260 cm^{-1} and 475 cm^{-1}, which are assigned for SnS and Cu_xS (particularly for S3 and S4) compounds, respectively (Sohila et al., 2011; Yeryukov et al., 2014). Although intense XRD diffraction peaks are detected for SnS phase as shown in Fig. 1, Raman spectra only revealed low intense peak possibly due to the limited penetration depth of the 455 nm wavelength laser, which was used as excitation source. Based on optical absorption coefficient (α) of monoclinic CTS determined by Crovetto et al. (2016), penetration depth ($L = 1/\alpha$) is calculated to be approximately about 60–70 nm. Sulphurization of Sn/CuSn metallic precursor most likely induced SnS deep in bulk of CTS film rather than on its surface, rendering ineffective detection of this particular binary phase.

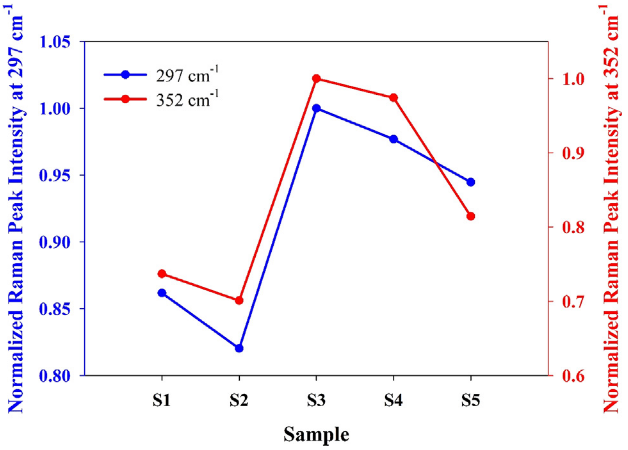

Fig. 5. Normalized CTS Raman peak intensity of all films.

(c) **Compositional analysis**

Elemental compositional measurement and analysis of all sulphurized films were carried out using EDX spectroscopy. Resulting atomic concentration, elemental ratio and percentage of Sn loss are shown in Table 2 and Fig. 6 and for ease of comparison, aforementioned results for concomitant metallic precursors are also included.

As noticeable, regardless of the initial Sn content in metallic precursors, sulphurization process induces CTS films with Cu/Sn ratio close to stoichiometric value of 2, meanwhile, S/metal ratio is close to unity. Only the S1 film shows mild Cu-rich composition (Cu/Sn = 2.05) while all the other films exhibit Cu-poor compositional characteristics (Cu/Sn = 1.86–1.98). Similar self-regulation of Cu/Sn ratio phenomenon has been previously reported by Johnson et al. during synthesis of CZTS films by sulphurization of co-sputtered Cu/CuZn/CuSn stacked metallic precursor (Johnson et al., 2015). The concept of Sn loss mechanism in Sn-S, Cu-Sn-S as well as Cu-Zn-Sn-S material systems has been long propounded and systematically investigated by Weber et al. (2010). In the mentioned pioneering work, it has been concluded that the observed Sn loss is due to evaporation of volatile SnS compound from the annealed thin film and particularly for Cu-Sn-S material system annealed at temperatures more than 460 and 480 °C, two distinct Sn loss mechanisms has been proposed as described in the reactions below:

$$2Cu_2SnS_3\ (s) \rightarrow Cu_4SnS_4\ (s) + \mathbf{SnS(g)} + S(g); \quad T > 460\ °C \tag{8}$$

$$Cu_4SnS_4\ (s) \rightarrow 2Cu_2S\ (s) + \mathbf{SnS(g)} + S\ (g); \quad T > 480\ °C \tag{9}$$

Since XRD measurement did not detect any diffraction peak indicating the existence of Cu_4SnS_4 phase, we conclude that both decomposition reactions of (8) and (9) and in aggregate are accountable for the observed Sn loss. Besides Sn loss through decomposition of primary Cu_2SnS_3 and secondary Cu_4SnS_4 phases as described above, additional Sn loss through direct decomposition of solid SnS phase to gaseous SnS specious is hypothesized to be at play as described in the reaction (10) below.

$$SnS(s) \rightleftharpoons \mathbf{SnS(g)} \tag{10}$$

Based on the XRD and EDX results, the following correlation can be inferred on the role of Sn content in CTS phase formation mechanism during sulphurization process. According to reaction (3), the binary compound of SnS_2 is the Sn-containing sulphide precursor responsible for the CTS formation upon reaction with Cu_2S. In the Sn/CuSn sequentially stacked metallic precursor configuration, SnS_2 phase has 2 distinct formation pathways; (i) from CuSn alloy precursor through reactions (1) and (2) and; (ii) from elemental Sn precursor through reaction (4). The SnS_2 phase originating from pathway (i) is most likely to be the primary source for Sn and fully consumed during crystallization of CTS due to shorter interatomic distance with Cu_2S. On the other hand, incorporation of the underlying SnS_2 phase resulting from pathway (ii) is assumed to be secondary, and is dependent on diffusivity

Table 2
Summary of EDX measurements for as-deposited precursors and sulphurized films.

Sample	Cu (%)	Sn (%)	S (%)	S/Metal	Cu/Sn	% of Sn loss
Precursor - Sn_25	61.01	38.99	–	–	1.5647	15.8502
Sulphurized - S1	34.39 (67.19)*	16.79 (32.81)*	48.82	0.9539	2.0482	
Precursor - Sn_65	55.75	44.25	–	–	1.2598	21.5593
Sulphurized - S2	33.46 (65.29)*	17.79 (34.71)*	48.75	0.9512	1.8808	
Precursor - Sn_170	52.22	47.78	–	–	1.0929	29.8033
Sulphurized - S3	34.51 (66.45)*	17.42 (33.54)*	48.08	0.9259	1.9811	
Precursor - Sn_260	51.48	48.52	–	–	1.0610	27.8648
Sulphurized - S4	33.25 (65.00)*	17.9 (35.00)*	48.85	0.9550	1.8575	
Precursor - Sn_310	47.54	52.46	–	–	0.9062	34.6169
Sulphurized - S5	33.27 (65.70)*	17.37 (34.30)*	49.36	0.9747	1.9154	

* (Normalized to Cu and Sn only).

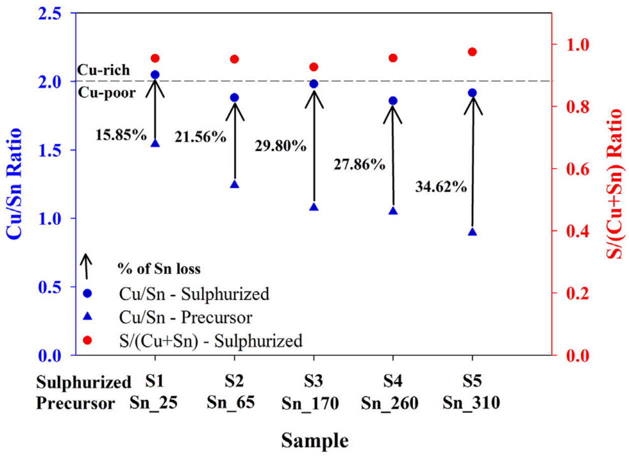

Fig. 6. Compositional ratio of as-deposited precursors and sulphurized films.

of SnS_2 into the existing Cu_2S-SnS_2 melt. However, either way effective incorporation of SnS_2 phase into the crystalizing host matrix will result in the enhancement of CTS structural property with Cu-poor, Sn-rich composition.

Remaining unreacted SnS_2 resultant from formation pathway (ii) will partially undergo a series irreversibly decomposition through reactions (5) and (6) to form crystalline SnS phase at the bottom of CTS film as detected by XRD. Finally, further decomposition through reaction (10) may take place and consequentially, inducing Sn loss in CTS films through evaporation of volatile SnS phase. Z. Tang et al. proposed similar growth model for CTSe through reaction path investigation by in-situ XRD method during selenization of sputtered Cu-Sn metallic precursor (Tang et al., 2015a). By re-examining Fig. 6, it can be said that CTS films of S1 (Cu/Sn = 2.05), S2 (Cu/Sn = 1.88) and S3 (Cu/Sn = 1.98) resulting from precursors of Sn_25 (Cu/Sn = 1.54), Sn_65 (Cu/Sn = 1.24) and Sn_170 (Cu/Sn = 1.09) exhibit progressive improvement in the crystallinity of CTS and SnS phases due to the beneficial effect of additional SnS_2 phase. However, CTS films of S4 (Cu/Sn = 21.85) and S5 (Cu/Sn = 1.88) resulting from precursors of Sn_260 (Cu/Sn = 1.04) and Sn_310 (Cu/Sn = 0.89) manifest lower CTS crystallinity compared to S3 (optimum), indicating deteriorating effect of excess SnS_2 phase due to SnS volatilization. This notion is further reinforced based on the observed degradation of SnS crystallinity (see Fig. 2) for S5 film, which also incidentally shows the highest percentage of Sn loss as depicted in Fig. 6. Therefore, initial content of elemental Sn in as-deposited metallic precursor dictates the effective incorporation of intermediate SnS_2 during CTS crystallization and the associated degree of Sn-loss.

(d) **Morphological and topological properties**

Figs. 7 and 8 illustrate the SEM morphologies and 2-D surface topographies, respectively. From the cross-sectional images, the thickness of CTS films is measured to be in between 1.93 (S1) to 2.57 µm (S5), and demonstrates anticipated linear relation with thickness of as-deposited metallic precursors (thus, Sn deposition time). The thickness of sulphurized films increased by about 140–180% compared to the corresponding thickness of metallic precursors. This expansion can be attributed due to the structural transformation of metallic Sn and CuSn precursors into SnS and CTS through incorporation of sulphur atoms

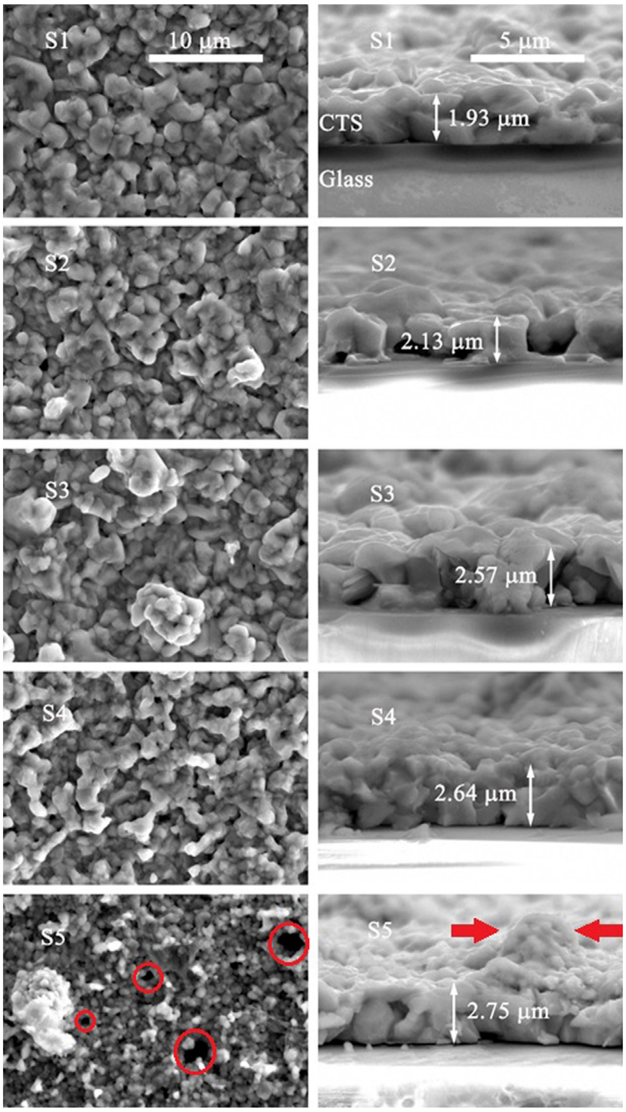

Fig. 7. Surface and cross-sectional morphology of CTS films.

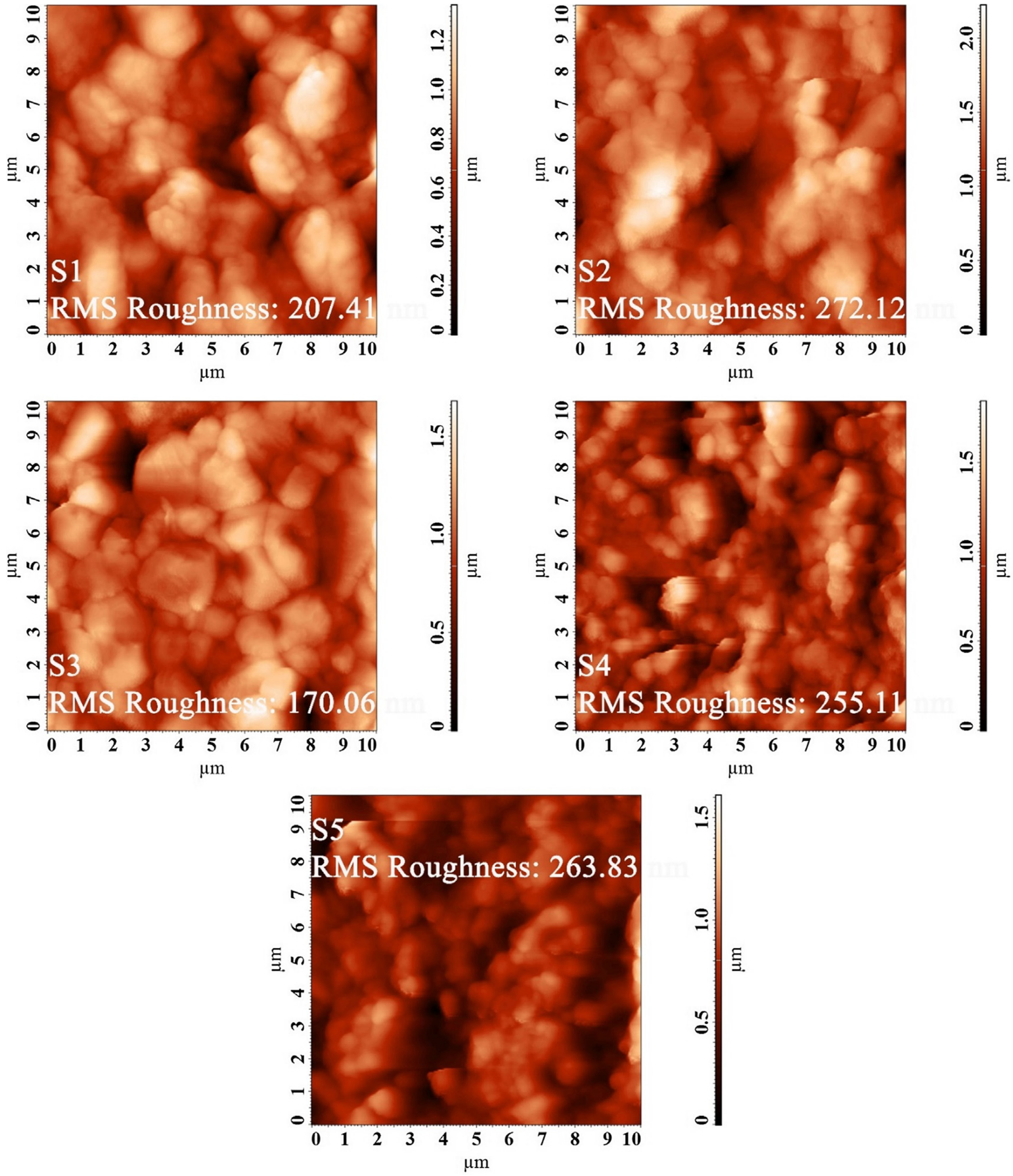

Fig. 8. 2-D topography and RMS roughness of CTS films.

during the sulphurization process. Cross-sectional view depicts columnar grain growth of micrometer range for all films, which is one of the desirable structural characteristics for photo-absorber layer due to its propensity to increase minority carrier diffusion length and collection positively (Zhang et al., 2014). S1, S2, and S3 films categorically exhibit similar surface microstructural properties namely compactness and grain shape. Distinct alteration in the surface microstructures is observed for S4 and S5 films compared to S1, S2, and S3 films. Gradual emergence of voids, formation of pin-holes and perceptible shrinkage in surface grain size are seen for S4 film and these observed microstructural degradations are substantially exacerbated in S5 film. Surface morphology of S5 film is composed of pervasive agglomeration of granular grains of nanoscopic scale and micrometer-sized pin-holes (red circles). Cross sectional view of S5 film exposes formation of dome-like microstructure (red arrows) most likely caused by pressure build-up from trapped SnS vapor, which is trying equilibrate during sulphurization pressure. Upon successful release of SnS vapor, this dome-like microstructure is transformed to micrometer sized pin-holes, thus increasing the porosity of the film as evident from the surface morphology view. SPM probed surface topographical characteristics of all sulphurized films as illustrated in Fig. 8 reveal good agreement with the obtained SEM morphology analysis. Markedly well-defined grain boundaries, compact surface microstructure and smaller voids are observed for S3 film compared S1 and S2 films, indicative of improved grain coalescence. As a resultant, S3 possesses lowest surface RMS roughness of 170.06 nm among all sulphurized films. Average surface RMS roughness values from this study is relatively higher compared to previous works mainly due to higher film thickness (Guddeti et al., 2018; Tiwari et al., 2013). In overall, morphological and topological properties of CTS films are reflective of the observed crystallinity trend and compositional analysis as presented earlier.

(e) Optical properties

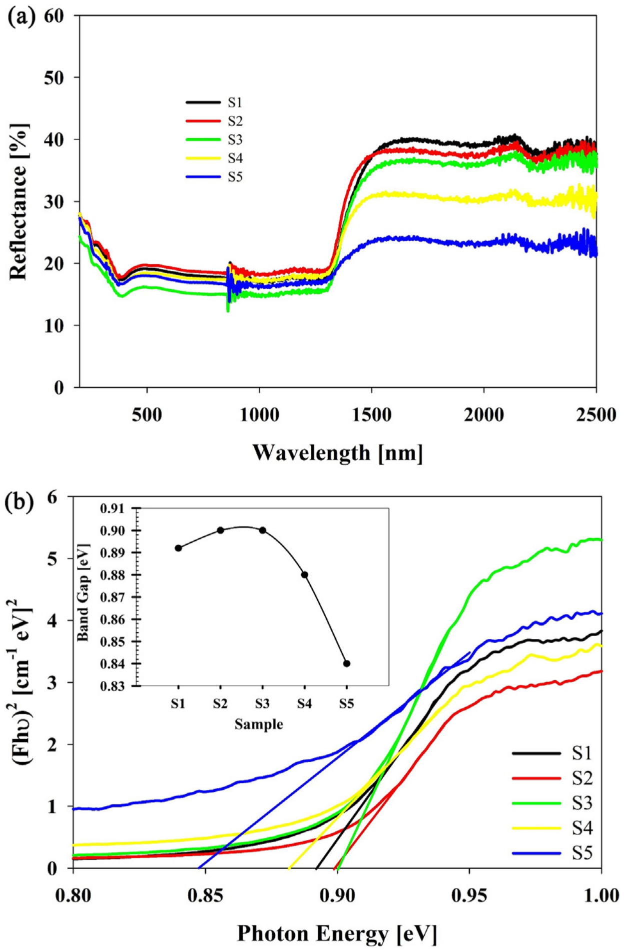

Fig. 9. Optical properties of CTS films (a) Reflectance spectra (b) Kubleka-Munk function plot for band gap determination (inset: band gap variation for of different CTS films).

Fig. 9(a) depicts the measured R spectra, which shows the distinct transition from low to high R value around 1350 nm. Brief seismic noise-like features in the R spectra at 800 nm is an artifact of merging data sets from different optical detectors. No obvious trend could be observed for R below wavelength of 1350 nm, however, S3 film notably records the lowest R among all CTS films in this region. On the other hand, for wavelength above 1500 nm, R decreases monotonically from S1 (Cu/Sn = 2.05) to S5 (Cu/Sn = 1.88). This systematic decrease in R is a direct evidence of the reduction in front surface reflection, most likely due to unintentional light trapping mechanism induced by formation and segregation of surface nanostructures, particularly in S4 and S5 films (Yang et al., 2013). In order to calculate the resulting optical band gap of CTS films, Kubleka-Munk (K-M or F(R)) method was applied. The K-M method is suitable for highly light scattering materials as well as absorbing particles and is based on the following equation (Kubelka and Munk, 1931),

$$F(R) = \frac{(1-R)^2}{2R} \tag{11}$$

where R is the reflectance. A modified Kubelka–Munk function can be obtained by multiplying the F(R) function by hυ as follows:

$$(F(R)*h\upsilon)^n \tag{12}$$

where υ is the frequency of photon, h is the Plank's constant, and using the corresponding coefficient n = ½ associated with direct allowed electronic transition. By plotting this equation as a function of the energy in eV and extrapolating the linear region of the curve to the horizontal axis, the band gap of semiconductor particles can be obtained as shown in Fig. 9(b) (López and Gómez, 2012) and inset plot therein. Similar to CTS crystallinity trend, S1, S2 and S3 films possess higher band gap values in the region of 0.89–0.90 eV compared to 0.88 eV for S4, and 0.84 eV S5 films, respectively. Decrement in the measured band gap values from 0.90 (S2 and S3) to 0.84 eV (S5) is most probably due to the reduced CTS crystallinity, which creates defect/tail states near the band edges and subsequently decreases the effective forbidden gap.

In general, band gap values for CTS films are determined to be in the range of 0.84–0.90 eV, which conform well with the theoretically calculated values (Zhai et al., 2011), although slightly lower than previous experimentally reported values for monoclinic CTS phase (de Wild et al., 2016b; Kanai et al., 2015; Raadik et al., 2017; Suzuki et al., 2017). Furthermore, any lingering ambiguity on the CTS phase identification through Raman spectroscopy due to the proximity of A_1 mode detected at 297 cm^{-1}, which is more often attributed to tetragonal phase is further dispelled through this optical band gap measurement, as tetragonal CTS is reported have a distinct band gap value of 1.35 eV (Fernandes et al., 2010; Wang et al., 2016).

(f) Electrical properties

Electrical properties of CTS films were measured by using Hall measurement and the resulting carrier concentration, Hall mobility, resistivity, Hall coefficient, and conductivity type are summarized in Table 3.

From the tabulated data, it can be seen that all CTS films exhibit consistent p-type semiconductor behavior with carrier concentration, Hall mobility, and resistivity in the range of 1.01×10^{18}–4.39×10^{18} cm^{-3}, 1.15–3.17 cm^2/V. s, and 0.99–4.18 Ω-cm, respectively. In the absence of extrinsic doping mechanism as in this study, the observed p-type conductivity and associated quantitative electrical parameters are most certainly to stem from intrinsic acceptor doping through formation native defects such copper vacancies V_{cu} and sulphur interstitial S_i (Zhao and Cheng, 2013). The highest carrier concentration and the lowest resistivity are recorded for S1 film, which can be ascribed to conductive Cu metallic-like phase, which may have formed due to its Cu-rich, Sn-poor composition (Cu/Sn = 2.05) (Bodeux et al., 2015). All the other films (S2 to S5), which are determined to be Cu-poor, Sn-rich exhibit minutely decreased carrier concentration and relatively higher resistivity compared to S1 film. Nonetheless, measured CTS carrier concentration and resistivity values in this study are in the region of low 10^{18} cm^{-3} and 0.99 Ω-cm < ρ < 4.18 Ω-cm, reflective of semiconducting property. Values measured from this study are significantly lower than 10^{19}–10^{20} cm^{-3} and

Table 3
Summary of electrical properties of CTS films obtained by Hall measurement.

Sample (Cu/Sn ratio)	Carrier concentration (n) (cm^{-3})	Hall mobility (μ) (cm^2/V·s)	Resistivity (ρ) (Ω-cm)	Hall coefficient (R_H) (m^3/C)	Type
S1 (2.05)	4.39E+18	1.43	0.99	1.43E+00	p
S2 (1.88)	1.30E+18	3.17	1.51	4.79E+00	p
S3 (1.98)	1.04E+18	2.72	2.21	6.02E+00	p
S4 (1.85)	1.79E+18	1.72	2.06	3.54E+00	p
S5 (1.91)	1.30E+18	1.15	4.18	4.80E+00	p

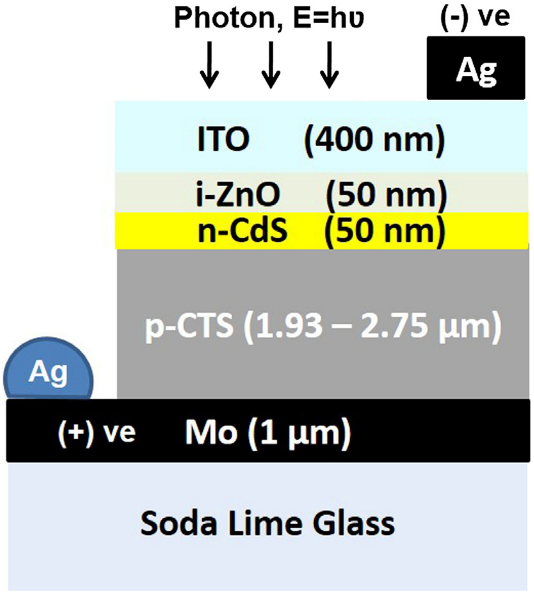

Fig. 10. Generic architecture of substrate type CTS thin film solar cell fabricated in this study.

higher than 10^{-2}–10^{-4} Ω-cm as reported previously in reference (Su et al., 2012) and are more suitable for thin film photovoltaic applications. S5 film registers the lowest Hall mobility of 1.15 cm^2/V. s and the highest resistivity of 4.18 Ω-cm, possibly due to higher density of microstructural imperfections such as voids, pin-holes, and grain boundaries as seen from SEM morphology, which may impede the charge carrier transport by scattering mechanism (Marcano et al., 2001).

Furthermore, Hall mobility of all CTS films fabricated in this study is considerably low compared to other equivalent monoclinic CTS films indicating further optimization is needed (Baranowski et al., 2015; Kim et al., 2017). The co-existence of secondary SnS phase, which can be classified as the impurity phase in the CTS films could be one of the contributing factors for the low mobility value.

(g) CTS thin film photovoltaic device

In order to establish a correlation between the elucidated material properties of 5 different CTS absorber layers, and their effects on photovoltaic conversion mechanism, all CTS samples (S1–S5) were further processed parallelly for thin film solar cell fabrication in the form of substrate type configuration as shown in Fig. 10. Each device consists of 8 individual cells, mechanically scribed to have an effective area per-cell of 0.25 cm^2 (Fig. S7 in the Supplementary Material shows the actual CTS devices).

Fig. 11 concisely shows the general trend with mean values that are denoted by circular symbols, meanwhile upper and lower limits of each plot represent maximum and minimum values. The S1 and S2 devices show comparable results with mean values of V_{oc} (110 mV), J_{sc} (7–8 $mAcm^{-2}$), FF (0.29) and efficiency (0.35%). Additionally, all measured parameters for both devices display the widest deviation from their respective mean values, suggestive of CTS absorber layers with spatial non-homogeneity. The S3 device exhibits the highest mean values for V_{oc} (150 mV), J_{sc} (10 $mAcm^{-2}$), FF (0.32, jointly with S2), and efficiency (0.71%), while the performance of S4 and S5 (has the lowest mean values for all parameters) devices gradually deteriorates. These obtained results come with no surprise as S3 film has consistently shown superior material properties compared to all the other films. Apart from the abovementioned unequivocal correlation, all the trend lines connecting consecutive mean values for all parameters (which serve as guides to the eye) show remarkable qualitative similarities with XRD (Figs. 1 and 2), Raman (Fig. 5), SEM (Fig. 7), and optical (inset of Fig. 9(b)) results' trends, further accentuating the interdependence between CTS films properties and device performance.

A preliminary attempt to increase the PCE of CTS device from S3 films was carried out through variation in sulphurization temperatures at 525 and 575 °C. However, the obtained device performances from these temperatures were inferior compared to best cell fabricated from S3 film sulphurized at 550 °C (see Fig. S8 in the Supplementary Material). Detailed investigation of impact of sulphurization temperature on CTS films was beyond the scope of our investigation during this experimental study, hence no further thin film material characterizations were carried out. Fig. 12. shows the dark and light J-V curves of the best cell from the S3 device, which records V_{oc} of 0.182 V, J_{sc} of 11.65 $mAcm^{-2}$, FF of 33.30 and subsequently 0.71% PCE. In comparison with the record performance of non Na-doped, sputtered deposited-pure sulfide CTS cell (V_{oc} = 0.243 V, J_{sc} = 26.20 $mAcm^{-2}$, FF = 47.9, PCE = 3.05%) reported by Chierchia et al. (2015), very low J_{sc} can be identified as the predominant loss factor in our cell.

Based on exhaustive results and discussion on CTS film material properties and the observed device characteristics as presented in preceding subsections, the following PCE limiting factors are highlighted and ensued by several propositions of prospective optimization routes for further improvement.

- **Phase pure CTS.** Ideally, pure-single phase CTS is desired for optimum device performance. However, in spite of having SnS secondary phase with pronounced crystallinity, S3 film produced the best performing device. On the other hand, S5 film which has the lowest crystallinity of SnS yielded device with the lowest PCE. This phenomenologically observed outcome is due to the fact that, decrement in SnS crystallinity in S5 film is due Sn loss mechanism, which in turn, induces deleterious surface microstructural features and outweighing the negative effects of SnS secondary phase itself. Therefore, straightforward elimination of SnS secondary phase through Sn loss mechanism is deemed detrimental and alternative route to incorporate SnS into CTS film effectively is highly sought. Hence, multi-period Sn/CuSn stacked precursor (Sn/CuSn × 2, Sn/CuSn × 3, etc.) configuration with appropriate thickness is proposed to promote inter-diffusion between elements for single phase CTS growth and circumvent the occurrence of excess SnS phase, which will inevitable decompose if it remains unreacted. On the other hand, alleviated Sn loss mechanism has been reported with the use of CuO-SnO2 oxide based precursor prepared by non-vacuum chemical process (Wang et al., 2018). This concept can be extended to vacuum based deposition technique for better uniformity and homogeneity control.

- **Absorber layer thickness.** Optically, for an absorber layer with $\alpha > 10^4\,cm^{-1}$, the thickness of 1 µm is sufficient for effective photon absorption while maintaining considerable J_{sc} value (Amin et al., 2012; Olle et al., 2003). Absorber layer with more than 1 µm do not necessarily renders higher J_{sc} and improved PCE, however, in contrary, could well result in lower V_{oc} due to increased carrier recombination in the quasi-neutral region (QNR) and subsequently inferior PCE (Scheer and Schock, 2011). Since, our preliminary emphasis in the precursor deposition step was to achieve Sn/CuSn metallic precursor with variable Cu/Sn ratio with the established sputtering process dynamics, no focus was given to the precursor thickness control. The thickness of our CTS absorber layers is the range of 1.93–2.75 µm (see Fig. 7), which is well above the optimum thickness considering the high absorption coefficient ($\alpha > 10^4\,cm^{-1}$) of monoclinic CTS (Crovetto et al., 2016). However, we believe that, by reducing the thickness of CTS film to about 0.8–1 µm while maintaining the optimum Cu/Sn ratio precursor (Sn_170) of 1.09, comparatively a higher PCE can be attained.
- **Minority carrier mobility and lifetime.** Photogenerated carrier collection potential of a photovoltaic absorber layer is interlinked to

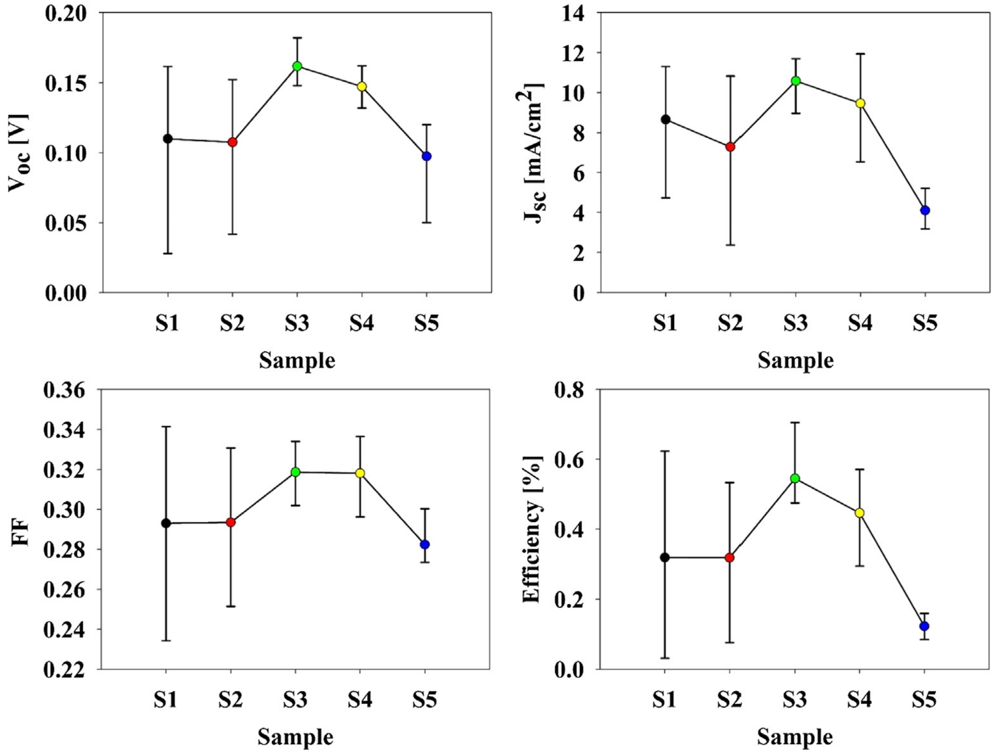

Fig. 11. Photovoltaic performance parameters of CTS thin film solar cells.

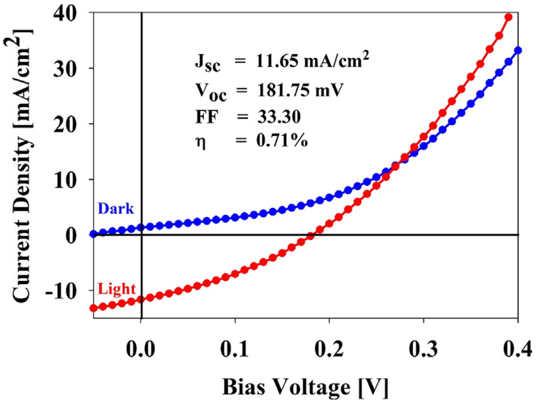

Fig. 12. Dark and light J-V curves of the best CTS cell from S3 device.

its basic semiconductor material properties namely carrier mobility μ and lifetime τ (Kirchartz and Rau, 2018). For a p-type thin film absorber layer, these 2 terms ultimately determine the minority carrier diffusion length of electron, $L_n = \sqrt{\frac{\mu_n \tau_n KT}{q}}$, where longer minority carrier diffusion length due to high μ_n and τ_n indicates increased probability of photogenerated carrier collection, thus, higher absorber layer quality (assuming partial depletion condition, $w/d < 1$, where w is the width of depletion region and d is the total thickness of absorber layer). Co-existence of SnS phase in absorber layer induces secondary heterojunction band line-up within bulk structure of CTS, which may perhaps have played disrupting role (mainly through blocking of carrier transport and increasing series resistance) during photogenerated charge carrier transport towards primary CdS/CTS heterojunction, consequently resulting in low μ_n and τ_n (Siebentritt, 2013). As mentioned earlier, our cells suffer from comparatively low J_{sc}, which could be due to the insufficient μ_n and τ_n to permit effective carrier collection. Hence, effective amalgamation of SnS phase into CTS as pointed out in the first point is crucial to improve the PCE.

- **Majority carrier concentration.** CTS films in this study exhibited relatively high majority carrier concentration, p in the region of $10^{18}\,\mathrm{cm}^{-3}$. Based on our previous work on CTS device performance assessment using AMPS-1D simulator, p of CTS absorber layer has a telling impact on the $V_{oc,}$ J_{sc} parameters and subsequently PCE (Hossain et al., 2018). Simulation results for cubic phase CTS ($E_g = 0.96$ eV) have been used as a reference for this case as it has the closest band gap to monoclinic CTS (S3; $E_g = 0.90$ eV). Our numerical analysis showed that 2.5 µm-thick CTS with p of $10^{15}\,\mathrm{cm}^{-3}$ (and carrier concentration of CdS; $n = 10^{18}\,\mathrm{cm}^{-3}$) produces the widest depletion region width of 1 µm, ensuring maximum photocurrent collection of more than 40 mAcm^{-2}. Drastic reduction in w is observed as p increased more than $10^{15}\,\mathrm{cm}^{-3}$ and at $p \geq 10^{18}\,\mathrm{cm}^{-3}$, w is calculated to be below 100 nm, which resulted in J_{sc} of about 10 mAcm^{-2}. Therefore, the collection probability of photogenerated carriers, which is readily being adversely affected by the higher thickness of absorber layer with a low value of L_n, now, is even further compounded by p-n heterojunction with a very narrow depletion region geometry. Apart from narrower depletion region, higher absorber layer doping compared to buffer layer doping ($N_{a,\ CTS} \gg N_{d,\ CdS}$) promotes CdS/CTS hetero-interface recombination. According to Niemegeers et al. (1995), as long as the hole concentration of absorber remains smaller than the electron concentration of buffer, interface defects states are completely occupied with electrons. However, when the hole density of absorber exceeds the electron density of buffer, then this scenario changes. Most of the defects states in the interface are now occupied by holes, which acts as electron traps in the interface region. These electron traps severely reduce the electron flow from the junction to the front electrode by interface recombination mechanism and substantially lowering the photocurrent. Controlling the charge carrier dynamics of CTS films can be achieved by reducing planar defects and cation disorder, through systematic investigation of annealing process (time, temperature and annealing ambient) as reported by Baranowski et al., who reported a lower p value of $8 \times 10^{17}\,\mathrm{cm}^{-3}$ with improved hole mobility for monoclinic CTS (Baranowski et al., 2015).

- **Surface roughness.** Uniform and smooth absorber layer with low surface roughness is imperative to form continuous p-n heterojunction with high-quality hetero-interface and subsequently better performing thin film photovoltaic device. Our CTS films exhibit high RMS surface roughness, which is less than ideal for uniform coverage of thin CdS buffer layer deposition during CBD process and therefore, affecting the built-in potential V_{bi}. Different thermal expansion coefficients of Sn and Cu_6Sn_5 metallic precursor as well SnS and Cu_2SnS_3 binary compounds (Collaboration: Authors and editors of the volumes III/17H-17I-41E () Cu2SnS3 crystal structure; Mu et al., 2011; Wiedemeier and Csillag Frank, 1979; Grey tin (alpha-Sn) thermal expansion), which could lead to non-homogenous lattice expansion during sulphurization is pinpointed as one of the reasons for high CTS film surface roughness. In order to reduce this effect, preheating of sputtered deposited metallic precursor at low temperature in absence of sulphur is recommended for homogenous intermixing of multi-elements prior to sulphurization process. Jiang et al. have successfully fabricated CZTS device with PCE of 8% by applying this method meticulously on electrodeposited Cu, Zn and Sn metallic precursors (Jiang et al., 2013). In their work, it was revealed that after sulphurization, precursors which underwent preheating step exhibited compact surface microstructures and smoother films with substantially reduced arithmetic average roughness compared to the non-preheated precursors.

4. Conclusion

In this study, CTS films were fabricated by sulphurization of sequentially sputtered Sn/CuSn stacked metallic precursors. The Cu/Sn ratio of the metallic precursor was intentionally altered (0.89–1.54) by varying elemental Sn layer thickness (25–310 nm) and its effects on the overall material properties of CTS films and device performance were investigated. It was revealed that precursor with Cu/Sn ratio of 1.09 (elemental Sn layer thickness of 65 nm) results in CTS films with overall optimum characteristics from various aspects of material properties such as crystallinity, surface morphology, roughness, optical band gap, and electrical parameters. Precursors with Cu/Sn ratio higher than 1.09 yielded CTS films with sub-optimal material properties due to higher Sn-loss during sulphurization. Unfavorable surface microstructural features such as pin-holes, non-homogenous morphology, and poor compactness were observed. Optimum CTS film (S3), which exhibited adventitious material properties led to the best CTS device with 0.71% PCE, thus, delineating the interdependence of absorber layer quality with photovoltaic performance. Several PCE retarding aspects from the context of CTS film properties, such as SnS secondary phase, absorber layer thickness, minority carrier dynamics, majority carrier concentration as well as surface roughness have been identified and relevant practical solutions are proposed.

Acknowledgment

Authors would like to acknowledge the Universiti Kebangsaan Malaysia (UKM) through its research grant MI-2018-007, Centre for Research and Instrumentation Management (CRIM) for its valuable contribution and extensive role in managing the material characterization systems as well as Institute of Sustainable Energy (ISE) of Universiti Tenaga Malaysia (@The National Energy Universiti) of Malaysia for their cordial support through BOLD2025 Program.

Appendix A. Supplementary material

Supplementary data to this article can be found online at https://doi.org/10.1016/j.solener.2018.10.081.

References

Grey tin (alpha-Sn) thermal expansion: Datasheet from Landolt-Börnstein - Group III Condensed Matter · Volume 41A1α: "Group IV Elements, IV-IV and III-V Compounds. Part a - Lattice Properties". In: SpringerMaterials. Springer-Verlag Berlin Heidelberg. https://dx.doi.org/10.1007/10551045_243.

Akio, S., Takahiro, W., 2018. First-principles studies on the interface between light-absorbing layer and Mo back electrode in Cu(In, Ga)Se_2, Cu_2 ZnSn(S, Se)$_4$, and Cu_2SnS_3 solar cells. Jpn. J. Appl. Phys. 57 (8S3), 08RC17.

Aliyu, M.M., Hossain, S., Husna, J., Dhar, N., Huda, M.Q., Sopian, K., Amin, N., 2012. High quality indium tin oxide (ITO) film growth by controlling pressure in RF magnetron sputtering. In: 2012 38th IEEE Photovoltaic Specialists Conference, pp. 002009–002013.

Amin, N., Chelvanathan, P., Hossain, M.I., Sopian, K., 2012. Numerical modelling of ultra thin Cu(In, Ga)Se_2 solar cells. Energy Proc. 15, 291–298.

Avellaneda, D., Nair, M.T.S., Nair, P.K., 2010. Cu_2SnS_3 and Cu_4SnS_4 thin films via chemical deposition for photovoltaic application. J. Electrochem. Soc. 157 (6), D346–D352.

Baranowski, L.L., McLaughlin, K., Zawadzki, P., Lany, S., Norman, A., Hempel, H., Eichberger, R., Unold, T., Toberer, E.S., Zakutayev, A., 2015. Effects of disorder on carrier transport in Cu_2SnS_3. Phys. Rev. Appl. 4 (4), 044017.

Baranowski, L.L., Zawadzki, P., Christensen, S., Nordlund, D., Lany, S., Tamboli, A.C., Gedvilas, L., Ginley, D.S., Tumas, W., Toberer, E.S., Zakutayev, A., 2014. Control of doping in Cu_2SnS_3 through defects and alloying. Chem. Mater. 26 (17), 4951–4959.

Berg, D.M., Djemour, R., Gütay, L., Siebentritt, S., Dale, P.J., Fontane, X., Izquierdo-Roca, V., Pérez-Rodriguez, A., 2012a. Raman analysis of monoclinic Cu_2SnS_3 thin films. Appl. Phys. Lett. 100 (19), 192103.

Berg, D.M., Djemour, R., Gütay, L., Zoppi, G., Siebentritt, S., Dale, P.J., 2012b. Thin film solar cells based on the ternary compound Cu_2SnS_3. Thin Solid Films 520 (19), 6291–6294.

Bodeux, R., Leguay, J., Delbos, S., 2015. Influence of composition and annealing on the characteristics of Cu_2SnS_3 thin films grown by cosputtering at room temperature. Thin Solid Films 582, 229–232.

Bouaziz, M., Ouerfelli, J., Srivastava, S.K., Bernède, J.C., Amlouk, M., 2011. Growth of Cu_2SnS_3 thin films by solid reaction under sulphur atmosphere. Vacuum 85 (8), 783–786.

Boydens, F., Leroy, W.P., Persoons, R., Depla, D., 2013. The influence of target surface morphology on the deposition flux during direct-current magnetron sputtering. Thin Solid Films 531, 32–41.

Chantana, J., Suzuki, K., Minemoto, T., 2017. Introduction of Na into Cu_2SnS_3 thin film for improvement of its photovoltaic performances. Sol. Energy Mater. Sol. Cells 168, 207–213.

Chelvanathan, P., Hossain, M.I., Amin, N., 2010. Performance analysis of copper–-indium–gallium–diselenide (CIGS) solar cells with various buffer layers by SCAPS. Curr. Appl Phys. 10 (3, Suppl.), S387–S391.

Chelvanathan, P., Rahman, K.S., Hossain, M.I., Rashid, H., Samsudin, N., Mustafa, S.N., Bais, B., Akhtaruzzaman, M., Amin, N., 2017a. Growth of MoOx nanobelts from molybdenum bi-layer thin films for thin film solar cell application. Thin Solid Films 621, 240–246.

Chelvanathan, P., Shahahmadi, S.A., Arith, F., Sobayel, K., Aktharuzzaman, M., Sopian, K., Alharbi, F.H., Tabet, N., Amin, N., 2017b. Effects of RF magnetron sputtering deposition process parameters on the properties of molybdenum thin films. Thin Solid Films 638, 213–219.

Chelvanathan, P., Shahahmadi, S.A., Ferdaous, M.T., Sapeli, M.M.I., Sopian, K., Amin, N., 2018. Controllable formation of MoS_2 via preferred crystallographic orientation modulation of DC-sputtered Mo thin film. Mater. Lett. 219, 174–177.

Chelvanathan, P., Zakaria, Z., Yusoff, Y., Akhtaruzzaman, M., Alam, M.M., Alghoul, M.A., Sopian, K., Amin, N., 2015. Annealing effect in structural and electrical properties of sputtered Mo thin film. Appl. Surf. Sci. 334, 129–137.

Chen, S., Gong, X.G., Walsh, A., Wei, S.-H., 2010. Defect physics of the kesterite thin-film solar cell absorber Cu_2ZnSnS_4. Appl. Phys. Lett. 96 (2), 021902.

Chierchia, R., Pigna, F., Valentini, M., Malerba, C., Salza, E., Mangiapane, P., Polichetti, T., Mittiga, A., 2015. Cu_2SnS_3 based solar cell with 3% efficiency. Phys. Stat. Sol. c 13 (1), 35–39.

Collaboration: Authors and editors of the volumes III/17H-17I-41E. Cu2SnS3 crystal structure, l.p., physical properties. In: Madelung, O., Rössler, U., Schulz, M., (Eds.), Ternary Compounds, Organic Semiconductors. Landolt-Börnstein - Group III Condensed Matter (Numerical Data and Functional Relationships in Science and Technology), vol. 41E. Springer, Berlin, Heidelberg.

Crovetto, A., Chen, R., Ettlinger, R.B., Cazzaniga, A.C., Schou, J., Persson, C., Hansen, O., 2016. Dielectric function and double absorption onset of monoclinic Cu_2SnS_3: origin of experimental features explained by first-principles calculations. Sol. Energy Mater. Sol. Cells 154, 121–129.

de Wild, J., Robert, E., Dale, P., 2016. Chemical Stability of the Cu2SnS3/Mo Interface.

de Wild, J., Robert, E.V.C., Adib, B.E., Abou-Ras, D., Dale, P.J., 2016. Secondary phase formation during monoclinic Cu_2SnS_3 growth for solar cell application. Sol. Energy Mater. Sol. Cells 157, 259–265.

Dong, Y., He, J., Sun, L., Chen, Y., Yang, P., Chu, J., 2015. Effect of sulfurization temperature on properties of Cu_2SnS_3 thin films and solar cells prepared by sulfurization of stacked metallic precursors. Mater. Sci. Semicond. Process. 38, 171–176.

Ferdaous, M.T., Chelvanathan, P., Shahahmadi, S.A., Sapeli, M.M.I., Sopian, K., Amin, N., 2018. Compositional disparity in Cu2ZnSnS4 (CZTS) thin film deposited by RF-sputtering from a single quaternary compound target. Mater. Lett. 221, 201–205.

Fernandes, P.A., Salomé, P.M.P., Cunha, A.F.D., 2010. A study of ternary Cu_2SnS_3 and Cu_3SnS_4 thin films prepared by sulfurizing stacked metal precursors. J. Phys. D: Appl.

Phys. 43 (21).

Fernandes, P.A., Salomé, P.M.P., da Cunha, A.F., 2011. Study of polycrystalline Cu_2ZnSnS_4 films by Raman scattering. J. Alloys Compd. 509 (28), 7600–7606.

Fürtauer, S., Li, D., Cupid, D., Flandorfer, H., 2013. The Cu–Sn phase diagram, Part I: New experimental results. Intermetallics 34, 142–147.

Guddeti, P.R., Gedi, S., Ramakrishna Reddy, K.T., 2018. Sulfurization temperature dependent physical properties of Cu_2SnS_3 films grown by a two-stage process. Mater. Sci. Semicond. Process. 86, 164–172.

Hossain, E.S., Chelvanathan, P., Shahahmadi, S.A., Sopian, K., Bais, B., Amin, N., 2018. Performance assessment of Cu_2SnS_3 (CTS) based thin film solar cells by AMPS-1D. Curr. Appl Phys. 18 (1), 79–89.

Husna, J., Aliyu, M.M., Islam, M.A., Chelvanathan, P., Hamzah, N.R., Hossain, M.S., Karim, M.R., Amin, N., 2012. Influence of annealing temperature on the properties of ZnO thin films grown by sputtering. Energy Proc. 25, 55–61.

Islam, M.A., Hossain, M.S., Aliyu, M.M., Chelvanathan, P., Huda, Q., Karim, M.R., Sopian, K., Amin, N., 2013. Comparison of structural and optical properties of CdS thin films grown by CSVT, CBD and sputtering techniques. Energy Proc. 33, 203–213.

Jiang, F., Ikeda, S., Harada, T., Matsumura, M., 2013. Pure sulfide Cu_2ZnSnS_4 thin film solar cells fabricated by preheating an electrodeposited metallic stack. Adv. Energy Mater. 4 (7), 1301381.

Johnson, M.C., Wrasman, C., Zhang, X., Manno, M., Leighton, C., Aydil, E.S., 2015. Self-regulation of Cu/Sn ratio in the synthesis of Cu_2ZnSnS_4 films. Chem. Mater. 27 (7), 2507–2514.

Kanai, A., Araki, H., Takeuchi, A., Katagiri, H., 2015. Annealing temperature dependence of photovoltaic properties of solar cells containing Cu_2SnS_3 thin films produced by co-evaporation. Phys. Stat. Sol. (b) 252 (6), 1239–1243.

Kang, J.-Y., Baek, G.Y., Gedi, S., Song, Y.J., Jeon, C.-W., 2018. Effects of the MoN diffusion barrier on the CZTSe growth behavior and solar cell performance. J. Alloys Compd. 748, 188–192.

Kim, J., Lee, J.Y., Jang, J., He, M., Jeong, W.-L., Suryawanshi, M.P., Yun, J.H., Lee, D.S., Kim, J.H., 2017. Influence of selenium doping on the properties of $Cu_2Sn(S_xSe_{1-x})_3$ thin-film solar cells fabricated by sputtering. Sol. Energy Mater. Sol. Cells 172, 154–159.

Kirchartz, T., Rau, U., 2018. What makes a good solar cell? Adv. Energy Mater. 1703385.

Kubelka, P., Munk, F., 1931. Ein beitrag zur optik der farbanstriche. Z. Techn. Phys. 12, 593–601.

Li, D., Franke, P., Fürtauer, S., Cupid, D., Flandorfer, H., 2013. The Cu–Sn phase diagram Part II: new thermodynamic assessment. Intermetallics 34, 148–158.

Lokhande, A.C., Chalapathy, R.B.V., He, M., Jo, E., Gang, M., Pawar, S.A., Lokhande, C.D., Kim, J.H., 2016. Development of Cu_2SnS_3 (CTS) thin film solar cells by physical techniques: a status review. Sol. Energy Mater. Sol. Cells 153, 84–107.

López, R., Gómez, R., 2012. Band-gap energy estimation from diffuse reflectance measurements on sol–gel and commercial TiO_2: a comparative study. J. Sol-Gel Sci. Technol. 61 (1), 1–7.

Luu, T.-T., Duan, A., Aasmundtveit, K.E., Hoivik, N., 2013. Optimized Cu-Sn wafer-level bonding using intermetallic phase characterization. J. Electron. Mater. 42 (12), 3582–3592.

Marcano, G., Rincón, C., de Chalbaud, L.M., Bracho, D.B., Pérez, G.S., 2001. Crystal growth and structure, electrical, and optical characterization of the semiconductor Cu_2SnSe_3. J. Appl. Phys. 90 (4), 1847–1853.

Matsumoto, Y., Aihara, N., Munemura, A., Tanaka, K., 2016. Preparation of monoclinic Cu_2SnS_3 single crystal by chemical vapor transport with iodine. Mater. Lett. 170, 213–216.

Mu, D., Read, J., Yang, Y., Nogita, K., 2011. Thermal expansion of Cu_6Sn_5 and $(Cu,Ni)_6Sn_5$. J. Mater. Res. 26 (20), 2660–2664.

Nagoya, A., Asahi, R., Wahl, R., Kresse, G., 2010. Defect formation and phase stability of Cu_2ZnSnS_4 photovoltaic material. Phys. Rev. B 81, 113202.

Niemegeers, A., Burgelman, M., De Vos, A., 1995. On the CdS/CuInSe2 conduction band discontinuity. Appl. Phys. Lett. 67 (6), 843–845.

Oliva, F., Arqués, L., Acebo, L., Guc, M., Sánchez, Y., Alcobé, X., Pérez-Rodríguez, A., Saucedo, E., Izquierdo-Roca, V., 2017. Characterization of Cu_2SnS_3 polymorphism and its impact on optoelectronic properties. J. Mater. Chem. A 5 (45), 23863–23871.

Olle, L., Marika, B., Jonas, M., Lars, S., 2003. Influence of the $Cu(In, Ga)Se_2$ thickness and Ga grading on solar cell performance. Prog. Photovol. Res. Appl. 11 (2), 77–88.

Pallavolu, M.R., Minnam Reddy, V.R., Pejjai, B., Jeong, D.-S., Park, C., 2018. Effect of sulfurization temperature on the phase purity of Cu_2SnS_3 thin films deposited via high vacuum sulfurization. Appl. Surf. Sci. 462, 641–648.

Pejjai, B., Minnam Reddy, V.R., Gedi, S., Park, C., 2017. Status review on earth-abundant and environmentally green Sn-X (X = Se, S) nanoparticle synthesis by solution methods for photovoltaic applications. Int. J. Hydrogen Energy 42 (5), 2790–2831.

Pejjai, B., Minnam Reddy, V.R., Gedi, S., Park, C., 2018. Review on earth-abundant and environmentally benign Cu–Sn–X(X = S, Se) nanoparticles by chemical synthesis for sustainable solar energy conversion. J. Ind. Eng. Chem. 60, 19–52.

Puvaneswaran, C., Mohammad Istiaque, H., Jamilah, H., Mohammad, A., Kamaruzzaman, S., Nowshad, A., 2012. Effects of transition metal dichalcogenide molybdenum disulfide layer formation in copper–zinc–tin–sulfur solar cells from numerical analysis. Jpn. J. Appl. Phys. 51 (10S), 10NC32.

Raadik, T., Grossberg, M., Krustok, J., Kauk-Kuusik, M., Crovetto, A., Bolt Ettlinger, R., Hansen, O., Schou, J., 2017. Temperature dependent photoreflectance study of Cu_2SnS_3 thin films produced by pulsed laser deposition. Appl. Phys. Lett. 110 (26), 261105.

Särhammar, E., Strandberg, E., Sundberg, J., Nyberg, H., Kubart, T., Jacobson, S., Jansson, U., Nyberg, T., 2014. Mechanisms for compositional variations of coatings sputtered from a WS2 target. Surf. Coat. Technol. 252, 186–190.

Sato, S., Sumi, H., Shi, G., Sugiyama, M., 2015. Investigation of the sulfurization process of Cu2SnS3 thin films and estimation of band offsets of Cu2SnS3-related solar cell structure. Phys. Stat. Sol. (c) 12.

Scheer, R., Schock, H.W., 2011. Design Rules for Heterostructure Solar Cells and Modules. Chalcogenide Photovoltaics.

Siebentritt, S., 2013. Why are kesterite solar cells not 20% efficient? Thin Solid Films 535, 1–4.

Sigmund, P., Oliva, A., Falcone, G., 1982. Sputtering of multicomponent materials: elements of a theory. Nucl. Instrum. Meth. Phys. Res. 194 (1), 541–548.

Sohila, S., Rajalakshmi, M., Ghosh, C., Arora, A.K., Muthamizhchelvan, C., 2011. Optical and Raman scattering studies on SnS nanoparticles. J. Alloys Compd. 509 (19), 5843–5847.

Su, Z., Sun, K., Han, Z., Liu, F., Lai, Y., Li, J., Liu, Y., 2012. Fabrication of ternary Cu–Sn–S sulfides by a modified successive ionic layer adsorption and reaction (SILAR) method. J. Mater. Chem. 22 (32), 16346–16352.

Suzuki, K., Chantana, J., Minemoto, T., 2017. Na role during sulfurization of NaF/Cu/SnS_2 stacked precursor for formation of Cu_2SnS_3 thin film as absorber of solar cell. Appl. Surf. Sci. 414, 140–146.

Takuya, K., 2017. $Cu(In, Ga)(Se, S)_2$ solar cell research in Solar Frontier: progress and current status. Jpn. J. Appl. Phys. 56 (4S), 04CA02.

Tang, Z., Aoyagi, K., Nukui, Y., Kosaka, K., Uegaki, H., Chatana, J., Hironiwa, D., Minemoto, T., 2015a. Reaction path for formation of Cu_2SnSe_3 film by selenization of Cu–Sn precursor. Sol. Energy Mater. Sol. Cells 143, 311–318.

Tang, Z., Kosaka, K., Uegaki, H., Chantana, J., Nukui, Y., Hironiwa, D., Minemoto, T., 2015b. Investigation on evaporation and suppression of SnS during fabrication of Cu_2SnS_3 thin films. Phys. Stat. Sol. (a) 212, 2289–2296.

Tiwari, D., Chaudhuri, T.K., Shripathi, T., Deshpande, U., Rawat, R., 2013. Non-toxic, earth-abundant 2% efficient Cu_2SnS_3 solar cell based on tetragonal films direct-coated from single metal-organic precursor solution. Sol. Energy Mater. Sol. Cells 113, 165–170.

Wang, C.-J., Shei, S.-C., Chang, S.-C., Chang, S.-J., 2016. Fabrication and sulfurization of Cu_2SnS_3 thin films with tuning the concentration of Cu-Sn-S precursor ink. Appl. Surf. Sci. 388, 71–76.

Wang, W., Cai, H., Chen, G., Chen, B., Yao, L., Dong, J., Yu, X., Chen, S., Huang, Z., 2018. Preparation of Sn loss-free Cu_2SnS_3 thin films by an oxide route for solar cell. J. Alloys Compd. 742, 860–867.

Weber, A., Mainz, R., Schock, H.W., 2010. On the Sn loss from thin films of the material system Cu–Zn–Sn–S in high vacuum. J. Appl. Phys. 107 (1), 013516.

Wiedemeier, H., Csillag Frank, J., 1979. The thermal expansion and high temperature transformation of SnS and SnSe. Zeitschrift für Kristallographie - Crystalline Materials 17.

Yan, C., Huang, J., Sun, K., Johnston, S., Zhang, Y., Sun, H., Pu, A., He, M., Liu, F., Eder, K., Yang, L., Cairney, J.M., Ekins-Daukes, N.J., Hameiri, Z., Stride, J.A., Chen, S., Green, M.A., Hao, X., 2018. Cu_2ZnSnS_4 solar cells with over 10% power conversion efficiency enabled by heterojunction heat treatment. Nat. Energy 3, 764–772.

Yang, Y., Green, M.A., Ho-Baillie, A., Kampwerth, H., Pillai, S., Mehrvarz, H., 2013. Characterization of 2-D reflection pattern from textured front surfaces of silicon solar cells. Sol. Energy Mater. Sol. Cells 115, 42–51.

Yeryukov, N.A., Milekhin, A.G., Sveshnikova, L.L., Duda, T.A., Pokrovsky, L.D., Gutakovskii, A.K., Batsanov, S.A., Rodyakina, E.E., Latyshev, A.V., Zahn, D.R.T., 2014. Synthesis and characterization of Cu_xS ($x = 1–2$) nanocrystals formed by the Langmuir-Blodgett technique. J. Phys. Chem. C 118 (40), 23409–23414.

Yusoff, Y., Chelvanathan, P., Huda, Q., Akhtaruzzaman, M., Alam, M.M., Al-Othman, Z.A., Amin, N., 2015. High quality CdS thin film growth by avoiding anomalies in chemical bath deposition for large area thin film solar cell application. J. Nanosci. Nanotechnol. 15 (11), 9240–9245.

Zawadzki, P., Baranowski, L.L., Peng, H., Toberer, E.S., Ginley, D.S., Tumas, W., Zakutayev, A., Lany, S., 2013. Evaluation of photovoltaic materials within the Cu-Sn-S family. Appl. Phys. Lett. 103 (25), 253902.

Zhai, Y.-T., Chen, S., Yang, J.-H., Xiang, H.-J., Gong, X.-G., Walsh, A., Kang, J., Wei, S.-H., 2011. Structural diversity and electronic properties of Cu_2SnX_3 (X = S, Se): a first-principles investigation. Phys. Rev. B 84 (7), 075213.

Zhang, H., Xie, M., Zhang, S., Xiang, Y., 2014. Fabrication of highly crystallized Cu_2SnS_3 thin films through sulfurization of Sn-rich metallic precursors. J. Alloys Compd. 602, 199–203.

Zhao, P., Cheng, S., 2013. Influence of sulfurization temperature on photoelectric properties Cu_2SnS_3 thin films deposited by magnetron sputtering. Adv. Mater. Sci. Eng. 2013, 1–4.